京都大学学術情報リポジトリ
KURENAI 紅
Kyoto University Research Information Repository

Physics of Plasmas

Ionization and acceleration of multiply charged gold ions in solid film irradiated by high intensity laser **EP**

D. Kawahito, and Y. Kishimoto

COLLECTIONS

EP This paper was selected as an Editor's Pick

open access

View Online   Export Citation   CrossMark

ARTICLES YOU MAY BE INTERESTED IN

Enhancement of proton acceleration and conversion efficiency by double laser pulses plasma interactions
Physics of Plasmas **27**, 033107 (2020); https://doi.org/10.1063/1.5143344

Plasma and trap-based techniques for science with antimatter
Physics of Plasmas **27**, 030601 (2020); https://doi.org/10.1063/1.5131273

Enhancing electromagnetic radiations by a pre-ablation laser during laser interaction with solid target
Physics of Plasmas **27**, 032705 (2020); https://doi.org/10.1063/1.5140585

Ionization and acceleration of multiply charged gold ions in solid film irradiated by high intensity laser

D. Kawahito[a)] and Y. Kishimoto[b)]

AFFILIATIONS

Graduate School of Energy Science, Kyoto University, Uji, Kyoto 611-0011, Japan

[a)]Author to whom correspondence should be addressed: dkawahito@ucsd.edu
[b)]kishimoto.yasuaki.8a@kyoto-u.ac.jp

ABSTRACT

In this paper, we present the mechanisms of ionization of a thin gold film irradiated by a high-intensity, short-pulse laser in the range of $I = 10^{20-22} \, \text{W/cm}^2$ and the associated acceleration of multiply charged gold ions. A numerical one-dimensional simulation using an extended particle-in-cell code, which includes atomic and collisional relaxation processes, indicates that two types of acceleration, hole-boring radiation pressure acceleration (RPA) and target normal sheath acceleration (TNSA), contribute to the generation of highly charged ions with kinetic energies on the order of 10 MeV/u. In each acceleration, a longitudinal electrostatic field excited by different mechanisms dominantly ionizes atoms to higher charge states and accelerates them to the vacuum region from the rear surface, which is opposite the front surface irradiated by the laser field. The field ionization process dominantly ionizes high energy ions to the high charge state, while a large number of ions with energy <1 MeV/u are ionized by an electron impact ionization process. In TNSA, a multiply charged ion generated at the rear surface is accelerated to the maximum energy although the ion with the highest charge state is generated at the front surface in RPA. However, the existence of contamination, such as water vapor, suppresses the ion energy of TNSA to less than that of RPA since the sheath field readily accelerates the protons and oxygen prior to the acceleration of the gold ions. Our derived theoretical scaling describes the maximum ion energy for each charge state in the cases with and without contamination using the relationship between the longitudinal electrostatic field profile near the rear surface and the classical tunnel field ionization model.

I. INTRODUCTION

Ion acceleration utilizing high-intensity laser interaction with a solid film has been studied for various applications, such as ion beam radiography,[1–5] ion beam therapy,[6,7] and fast ignition using a proton beam.[8,9] In this scheme, proton acceleration has been studied intensively, as it has the highest charge-to-mass ratio among all atoms, leading to the generation of high energy ions. In experiments based on the above scheme, protons contained in water vapor attached on a film surface are accelerated to high energies on the order of sub-10 MeV/u within a short time ($\simeq 1$ps) and within a small area ($\simeq 10 \mu$m).

In similar experiments using higher intensity lasers, not only protons but also heavier ions with nearly fully stripped charge states, which originate from the bulk material constituting the film (e.g., carbon,[10] aluminum,[11] and iron[12]), have also been observed with high energies on the order of sub-10 MeV/u. These results indicate that the scheme for accelerating protons is worthwhile to be extended to a

scheme for accelerating bulk heavier ions with high charge states, which is relevant to a broader class of applications in addition to proton acceleration, such as a highly charged heavy ion injector for nucleus–nucleus collisions[13,14] and nuclear transmutation[15,16] and extraction and acceleration of short-lived exotic nuclei.[17,18]

For either proton acceleration or heavy ion acceleration, the generation of high energy electrons plays an important role in regulating ion acceleration to high energies.[19,20] Namely, as the laser intensity increases to above $I = 1.36 \times 10^{18}/\lambda(\mu$m$) \, \text{W/cm}^2$, where the accelerated electron energy reaches the relativistic regime, the accelerated ion energy also increases significantly.[21–23] The generation of high energy electrons is ascribed to the ion acceleration by the electric sheath field, which is referred to as target normal sheath acceleration (TNSA).[24,25] In TNSA, high energy electrons accelerated by the laser field around the front surface of the film induce a quasi-static electric field around the rear surface due to charge separation. The sheath field accelerates

ions to high energies.[26,27] Direct ion acceleration from the front surface also takes place and becomes an important process for regulating ion energies emitted from the rear side, especially for higher laser intensities as mentioned above. Namely, a quasi-static electric field is induced around the front surface of the film toward the inside due to electrons being pushed by the laser ponderomotive force, which also accelerates ions toward the inside. This mechanism is nearly identical to the hole-boring radiation pressure acceleration (RPA),[28–30] which is proposed for ion acceleration using ultra-thin films.

These two mechanisms are considered to be the basis even when the scheme is extended to heavy ion acceleration, as it is also achieved by an induced quasi-static longitudinal electric field. However, in heavy ion acceleration, the ionization process is of particular importance since the interaction is initiated from the neutral state and/or lower charged states due to the laser prepulse component, and it proceeds with different time scales depending on the mechanism (e.g., ionization by the laser field and ionization by electron impact). Namely, the resultant electron energy distribution, which regulates the generation of the quasi-static electric field, sensitively depends on the complex ionization process. In addition, multiple charge state distributions generated by laser interaction complicate the acceleration mechanisms due to the difference in the charge to mass ratios. These features suggest that a fully self-consistent treatment including all of the above-mentioned elementary processes is required to analyze both ionization and acceleration of heavy ions through laser interaction.

In this paper, using the particle-based integrated code (EPIC),[31] we study the interaction between a high-intensity laser in the range of $I = 10^{20-22}$ W/cm^2 and a gold (Au) film and the resultant acceleration dynamics of Au ions with different charge states. The EPIC is a particle-in-cell code that includes key ionization processes, such as field ionization and electron impact ionization. All collisional effects among the same and different species of charged particles (e.g., electrons and different charge state ions) are incorporated using a Monte Carlo scheme. As a result, it is possible to simulate the complex generation process of heavy ion plasma irradiated by a high-intensity laser, which exhibits highly nonlinear and non-stationary dynamics.

Based on the PIC simulation, we investigate the effect of the two above-mentioned acceleration mechanisms (TNSA from the rear side and hole-boring RPA from the front side) on the multiple ion charge distributions through the ionization processes. Two ion groups accelerated by each mechanism evolve differently in the vacuum region of the rear side, leading to different charge distributions. For the TNSA, which works on the rear side, we successfully derive the theoretical scaling of the maximum ion energy for each charge state. However, the energy distribution is found to be sensitively influenced by the existence of contamination such as water vapor (H$_2$O).

This paper is organized as follows: In Sec. II, we present physical principles underlying the models used in the EPIC to describe the ionization and relaxation processes. In Sec. III, we present the one-dimensional simulation results in the case of a laser intensity of $I = 10^{21}$ W/cm^2 and discuss the fundamental properties for ionization and acceleration. In Sec. IV, we discuss the dependence of the accelerated maximum ion energy on the irradiated laser intensity, while in Sec. V, we examine the effect of the contamination layer on the ion energy distributions. In Sec. VI, we derive the scaling model for the maximum ion energy of each charge state and compare it with simulation results. In Sec. VII, we discuss the effect of collisional

ionization and three-body recombination on ion acceleration. We provide conclusions in Sec. VIII.

II. SIMULATION MODEL INCLUDING IONIZATION AND RELAXATION PROCESSES

In this section, we describe the model used in the EPIC, which includes a collisional relaxation process and an ionization process. We also discuss the parameters used in the present simulation for studying the interaction between a high-intensity laser and a thin film consisting of a heavy atom. We select Au with atomic number $Z = 79$. Its electron configuration is [Xe] $4f^{14}5d^{10}6s^1$, where [Xe] is the electron configuration of xenon. Two processes for ionization are considered in this code: field ionization and electron impact ionization. The effect of three-body recombination estimated by the post-process calculation is discussed in Sec. VII and is found to be negligibly small.

Ionization of a heavy high-Z material irradiated by a high-intensity laser exhibits more complex features than those exhibited by a low-Z material. Ionization sensitively depends on the bound energy specific to the atom, which is densely packed in a high-Z atom and exhibits wider bandgaps associated with the jump of the principal quantum number n. This feature can be observed from the ionization energy distribution of the Au atom for the charge state q (i.e., U_q), which is illustrated in Fig. 1. The dashed lines in Fig. 1 represent the ionization energy for the outermost charge state for each principal quantum number n. The figure also represents the corresponding laser intensity that ionizes the gold atom due to the field ionization estimated from $I_{thr} = 1.0 \times 10^9 U_q^4 q^{-2}$ W/cm^2,[32] which represents the threshold value for the laser intensity that ionizes all electrons to a higher charge state than the corresponding principle quantum number n. For a laser intensity of $I \geq 10^{21}$ W/cm^2, which is the typical value in this study, the achieved ionization state is estimated to be $q = 65$ (3p). However, the process is more complex since both the electron impact ionization and the ionization due to various fields in the material regulated by the surrounding plasma lead to multiple charge distributions and corresponding ion energy distributions.

To include the ionization process in the particle-in-cell code, a Monte Carlo scheme is employed by evaluating the cross section for each process, that is, the ADK model[33] for field ionization and the
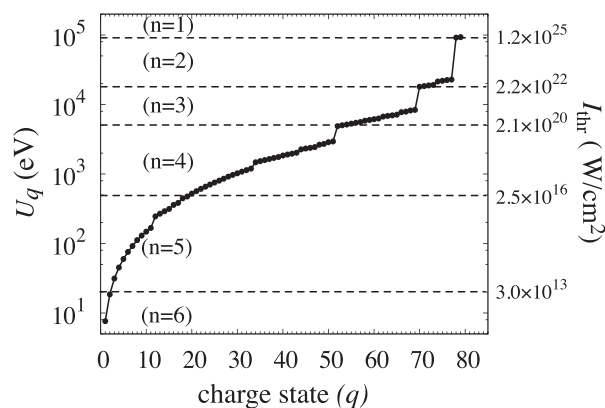

FIG. 1. Ionization energy for each charge state U_q of Au up to $q = 79$. A dashed line represents the ionization energy of the outer-shell electron for each principal quantum number n and the corresponding threshold laser intensities I_{thr} (W/cm^2).

BEB model[34] for electron impact ionization. These ionization processes are incorporated with collision processes between the same species (e.g., electron–electron and ion–ion with the same charge state q) and different species (e.g., electron–ion and ion–ion with a different charge state $q - q'$), which are based on the pairing method.[35,36] The scattering angle in the collision between the same species is estimated from the binary collisional process based on the collisional frequency in Spitzer thermal theory,[37]

$$\nu_{e-i} = \frac{4\pi n q^2 e^4}{m_e^2 \gamma^2 v_e^3} \ln\left(\frac{\lambda_D}{b_{\min}}\right), \qquad (1)$$

where n is the ion density, v_e is the electron velocity, γ is the relativistic factor for v_e, and m_e is the electron mass. λ_D is the Debye length, which is approximated by a mesh size, and b_{min} is the minimum impact parameter, which approximated to $h/\gamma m_e v_e$ from Planck constant h as the de Broglie wavelength. Here, we extend the Coulomb logarithmic term for the collision between an electron and a partially charged ion as follows:

$$\nu_{e-i} = \frac{4\pi n e^4}{m_e^2 \gamma^2 v_e^3} \left[q^2 \ln\frac{\lambda_D}{a_q} + q_{\max}^2 \ln\frac{a_{(q_{\max}-1)}}{b_{\min}} + \sum_{q'=q+1}^{q_{\max}-1} q'^2 \ln\frac{a_{(q'-1)}}{a_{q'}} \right], \qquad (2)$$

where a_q is the Bohr radius estimated by ionization potential, $a_q = 2U_q/qe^2$. It is noted that q is the outer charge state. In $b_{min} < a_Z$, q_{max} is determined by the fully ionized state, $q_{max} = Z$, where Z is the ion atomic number. In $a_{q''+1} < b_{\min} < a_{q''}$, q_{max} is determined by a partially ionized state, $q_{max} = q''$. This approach can reproduce transient (non-stationary) plasma dynamics in a self-consistent manner, in which ion charge state distributions change rapidly under the influence of a high-intensity short-pulse laser. Specifically, for a heavy ion acceleration from a substrate high-Z film such as gold, the collisional relaxation process and the resultant collisional ionization play an important role to decide the plasma parameters of the bulk density and the temperature.

We have calculated the interaction between a thin gold film and a short-pulse laser using the EPIC, whose configurations are the same as those used in Ref. 30. Namely, the simulations were performed in the one-dimensional domain of $-3.2\,\mu m \leq y \leq 16.8\,\mu m$ in the y-direction. A linearly polarized short-pulse laser with electric and magnetic fields in the x- and z-directions, respectively, is irradiated along the y-direction by an antenna placed at $y = -3.1\,\mu m$ near the LHS boundary.

The Au film with constant density n_1 is set at $y_1 \leq y \leq y_2$, where $y_1 = 0.0\,\mu m$, such that y_2 corresponds to the effective thickness of the film. A pedestal (pre-plasma) with a density that gradually increases from n_0 to n_1 as $n(y) = n_1 \exp(-(y_1 - y)/L_p)$ in $y_0 \leq y \leq y_1$ is assumed, where $L_p = 0.08\,\mu m$. Here, the density at the front (i.e., $n_0 = n(y_0) = pn_1$) is determined by $p = 10^{-3}$. The density of the Au film is selected to be the real value given by $n_1 = 6.0 \times 10^{22}$ cm^{-3}. The number of the macro-ion particles is set to 500/mesh. The corresponding macro-electron number is $q \times 500$/mesh with the same particle weight to the ion.

The laser wavelength is $\lambda_\ell = 0.8\,\mu m$, and the corresponding cut-off density in the non-relativistic limit is given by $n_c = 1.74 \times 10^{21}$ cm^{-3}. The laser pulse width is selected to be $\tau_\ell = 40$ fs with a

Gaussian form $\exp\left[-4(t - t_p)^2/\tau_\ell^2\right]$, where $t_p = 80$ fs, which is the time at which the laser intensity reached a peak value. The maximum laser intensity is typically set to $I = 1.0 \times 10^{21}$ W/cm^2, which corresponds to $a_0 (\equiv eA_0/mc^2) = 21.9$ in normalized units. The mesh number and width in the y-direction are $N_y = 4000$ and $\Delta y = 5.0 \times 10^{-3}\,\mu m$, respectively. To describe the collisional ionization in the high-density plasma, a small time step is required. In $\Delta t > 0.6\Delta y/c$, it was confirmed that the numerical divergence takes place in our test simulations. Therefore, we set the time step $\Delta t = 0.1\Delta y/c$, which also satisfies the Courant–Friedrichs–Lewy (CFL) condition $\Delta t < \Delta y/c$.

III. SIMULATION RESULTS OF IONIZATION AND ACCELERATION

In this section, we show the simulation results of the ionization dynamics and the acceleration of the multiply charged ions in the laser interaction with the Au film. Figure 2(a) illustrates the temporal evolution of each energy averaged over the system, specifically the field energy E_f, including the electrostatic and electromagnetic components, the electron kinetic energy E_e, the ion kinetic energy summed over all different charge states $E_i (= \sum_{q=1}^{79} E_i^{(q)})$ (where $E_i^{(q)}$ is the ion energy for the charge state q), the energy E_t defined by $E_t = (E_f + E_e + E_i)$,

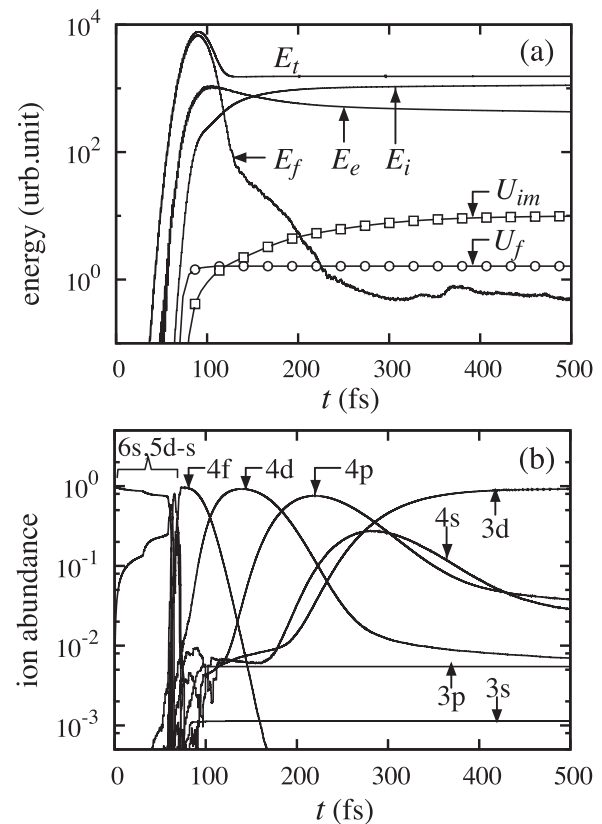FIG. 2. (a) Solid lines represent the temporal evolution of field $E/_f$, electron energy E_e, and ion energy E_i. Dotted lines represent the temporal evolution of field ionization loss U_f and electron impact ionization loss U_{im}. E_t represents the total energy $E_t = E_f + E_e + E_i$. (b) Time history of ion abundance for each subshell (s, p, d, and f) of each principal quantum number n.

the ionization energy due to the field $U_f (= \sum_{q=1}^{79} U_f^{(q)})$, and the electron impact $U_{im}(= \sum_{q=1}^{79} U_{im}^{(q)})$. Figure 2(b) illustrates the temporal evolution of ion abundance in each subshell (s, p, d, and f) of each principal quantum number n. As the low-power pedestal of the laser field (i.e., $I < 10^{16}$ W/cm^2) hits the film, the outer shell electrons (i.e., those of 6s and 5d states) are ionized, leading to ions with Au^1 $-$ Au^{11}. As the laser intensity increases to the peak value at $t = 100$ fs (i.e., 10^{21} W/cm^2), ionization proceeds further, leading to Au^{12} $-$ Au^{20}. Then, both E_t and E_f are dropped down since the reflected laser field escapes to the outside of the simulation box from the left-hand boundary. Free electrons produced by these ionization processes directly interact with the laser and obtain energy (i.e., E_e). The energy saturates after the peak of laser irradiation, $t \simeq 100$ fs, and then gradually decreases, as seen in Fig. 2(a). The ion energy E_i increases to be higher than the electron energy (i.e., E_e) at $t \simeq 160$ fs, while both energies E_i and E_e lead to almost constant values at a later time $t = 500$ fs. It is noted that the field energy, E_f, is not completely diminished but survives transiently, exhibiting a weaker damping (i.e., nearly exponential damping), as seen in 160 fs $< t <$ 220 fs in Fig. 2(a). This results from the formation of electrostatic sheath fields due to high-energy electrons around the front and rear sides of the film. The increase in E_i results from the acceleration of multiply charged ions due to the sheath fields, whose details are discussed in Sec. III A. It is also noted that ionizations to 4d, 4p, and 4s states continue after the laser irradiation, leading to the 3d state (Au^{52} $-$ Au^{61}) at $t = 500$ fs, as illustrated in Fig. 2(b). A small number of 3p and 3s states (Au^{62} $-$ Au^{69}) are produced during the laser irradiation of $t \simeq 100$ fs while keeping almost constant values at later times.

At $t = 500$ fs, when each energy saturates, the total absorption ratio is estimated by $E_t(t = 500 \text{ fs})/W_L = 0.21$, where W_L is the irradiated laser energy. The ratios of the field ionization energy, U_f $(t = 500 \text{ fs})/W_L$, and electron impact ionization energy, U_{im} $(t = 500 \text{ fs})/W_L$, are only 8.0×10^{-4} and 4.0×10^{-3}, respectively. Thus, the effect of ionization loss is negligible for both the plasma absorption energy and the ion acceleration mechanism. However, the temporal evolution shows each ionization process. The field ionization saturates at $t = 90$ fs, which corresponds to the time at which the laser reaches the peak intensity, while electron impact ionization continues. Therefore, both ionization components have an important role to determine the charge state of the accelerated ions.

Figure 3 represents the ratio of the ionization components of the field (a) $\bar{N}_f^q = N_f^q/N_{ion}$ and the electron impact (b) $\bar{N}_{im}^q = N_{im}^q/N_{ion}$ at $t = 500$ fs when the ionization saturates, where $N_{f,im}^q$ are the ion abundance ionized by the field (f) and impact (im) for each charge state q and N_{ion} is the total ion number. The ratios are divided into four groups from the initial location of the film as follows: (i) $0.0 \,\mu m \le y < 0.2 \,\mu m$, (ii) $0.2 \,\mu m \le y < 0.4 \,\mu m$, (iii) $0.4 \,\mu m \le y < 0.6 \,\mu m$, and (iv) $0.6 \,\mu m \le y < 0.8 \,\mu m$. As seen in Fig. 3(a), ionization to q = 18 (5s) is dominantly determined by the field even on the inside of the film. This is due to the ionization wave co-propagating with the electrostatic field excited by high energy electron bunches. Around t = 30 fs, the laser intensity irradiated on the front surface of the film reaches the electron relativistic regime in which the electrons are accelerated over MeV. Then, the high energy electrons start to propagate toward the inside as the bunch and excite the electrostatic field on the propagation front. This field ionizes the ions inside of the
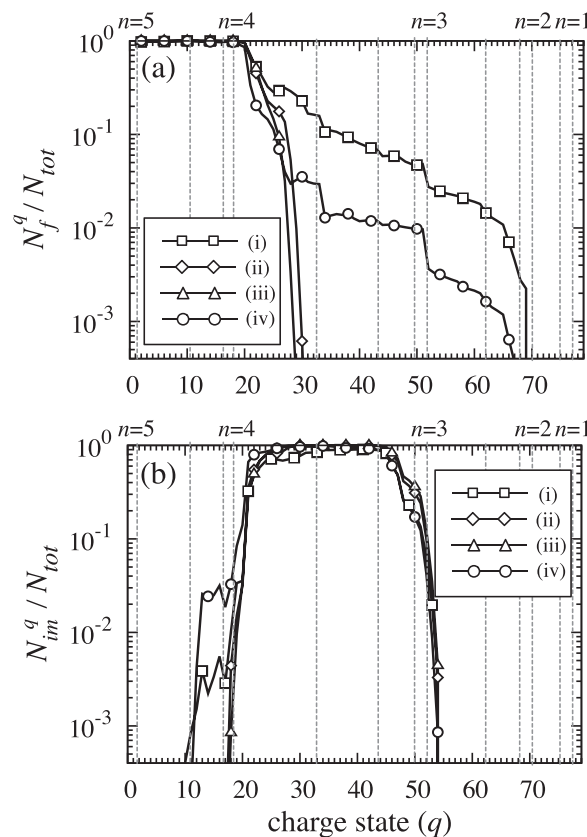

FIG. 3. Ionization ratio generated by (a) the field and (b) electron impact at $t = 500$ fs. Here, the ratios are divided into four groups from the initial location of the film: (i) $0.0 \,\mu m \le y < 0.2 \,\mu m$, (ii) $0.2 \,\mu m \le y < 0.4 \,\mu m$, (iii) $0.4 \,\mu m \le y < 0.6 \,\mu m$, and (iv) $0.6 \,\mu m \le y < 0.8 \,\mu m$.

film before the collisional ionization takes place since the mean free path of the accelerated electron bunches with the energy over MeV is much longer than the film thickness ($\gg 0.8 \,\mu$m). The electron bunch continues to be injected every half period of the laser oscillation, and the electric field ionizing the ions inside of the film keeps a certain amplitude to ionize the whole ions over $q = 18$ (5s). The detail mechanism of the field ionization inside the material is also discussed in Ref. 31. However, the field ionization decreases for the higher charge states, and the ratios of the inside parts (ii) and (iii) saturate to $q = 30$ (4f) and $q = 29$ (4f), respectively. A few numbers of ions on the front side (i) are ionized to a higher charge state to $q = 69$ (3s) since the laser field directly interacts with the film surface. The field ionization on the rear side (iv) also proceeds to a high-charge state $q = 67$ (3d) due to the excitation of the sheath field on the rear surface of the film. These results indicate that ionization to a high-charge state of $n = 3$ proceeds around both surfaces through different field ionization dynamics. On the other hand, most of the ions are ionized to $q = 18$ (5s)-54 (3s) by the electron impact in the entire region, as seen in Fig. 3(b). The total ratio of the electron impact is much larger than that of the field. In the interaction, when the laser pulse hits the surface of the film, the field starts to ionize the plasma first. Both the energy and the density of the generated electron increase with the increase in the irradiated laser
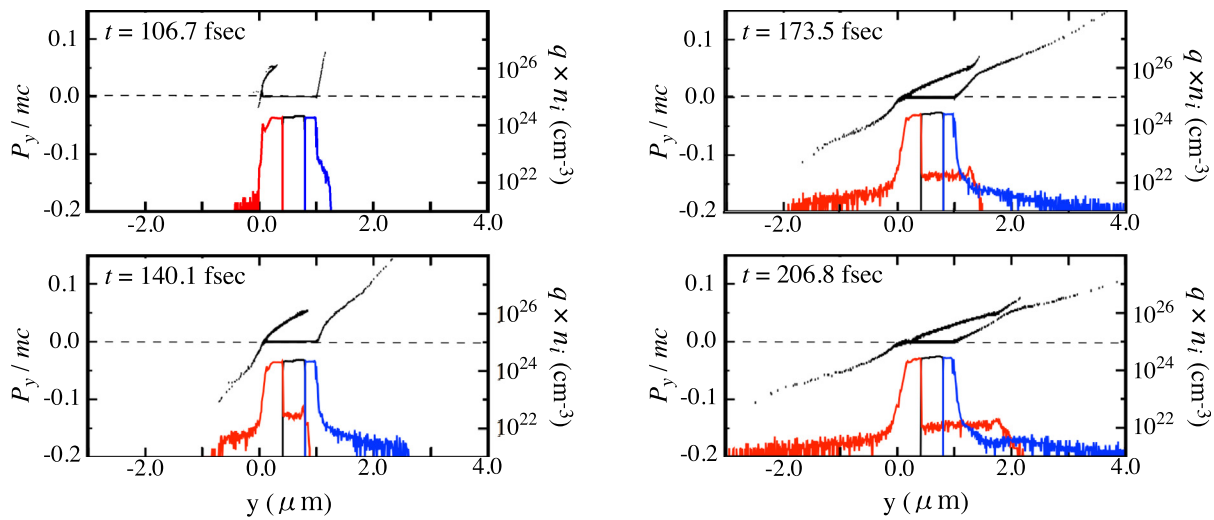
京都大学
KYOTO UNIVERSITY

Physics of Plasmas

ARTICLE

scitation.org/journal/php

京都大学学術情報リポジトリ
KURENAI 紅
Kyoto University Research Information Repository

FIG. 4. Spatial distributions of ion phase space and ion charge density. The ion density is categorized by the initial location on (i), (ii) + (iii), and (iv) as indicated by red, black, and blue lines, respectively.

intensity. After the electron energy becomes high enough to further ionize the gold ions, the collisional ionization subsequently starts to proceed in the inside of the film target. Therefore, the electron impact ionization starts later than the field ionization, which is driven immediately by the laser irradiation.

The acceleration mechanisms from both surfaces generate high energy and highly charged ions. Figure 4 represents the phase space of the ion momentum $y - p_y/M_i c$ and the spatial distributions of the ion charge density $q n_i$, which are categorized by the spatial film region of (i), (ii) + (iii), and (iv) at the representative times. In the phase space, two types of ion acceleration processes take place from the front and rear surface. From the front surface, the ions start accelerating toward the inside via hole-boring RPA at $t = 106.7$ fs, and the ion momentum then increases to $p_y/M_i c = 0.05$. It is noted that the ions are not only accelerated in the $+y$ direction from the front surface but also expanded in the $-y$ direction due to the sheath field. These ions for $p_y \geq 0$ ballistically propagate to the inside of the film, keeping the accelerated ion speed. When the ions are emitted from the rear surface of the film, the local density of the accelerated ions is larger than that of (iv). Therefore, secondary charge separation takes place on the accelerated ion front of (i) behind the expanded ions of (iv), and the electric field then re-accelerates the ions to $p_y/M_i c = 0.07$. In addition, the ions around the rear surface are also accelerated to the right-hand side vacuum area via TNSA. The ions continue to be accelerated as long as the sheath field survives, as illustrated in Fig. 2(a). At $t = 206.8$ fs, the peak momentum of (iv) increases to $p_y/M_i c = 0.15$, which corresponds to roughly twice the energy of (i). These acceleration mechanisms are closely related to the ionization process for the accelerated ions. The details of the ionization and energy distribution for each mechanism are discussed in Secs. III A and III B, respectively.

A. Hole-boring RPA with the ionization process

To discuss the acceleration from the front surface, we show the charged ion distributions $n_i^{(n,l)}$ for the region of (i) + (ii) + (iii) on a logarithmic scale, which is categorized by principal quantum number n and subshell $l = (s, p, d, f)$, and the electric field for the laser propagation direction E_y on a linear scale in Fig. 5. The ions near the front surface are ionized following the laser profile, which forms a standing wave consisting of the incident and reflected laser components. The highest charge state $q = 69$ (3s) is generated in front of the cut-off
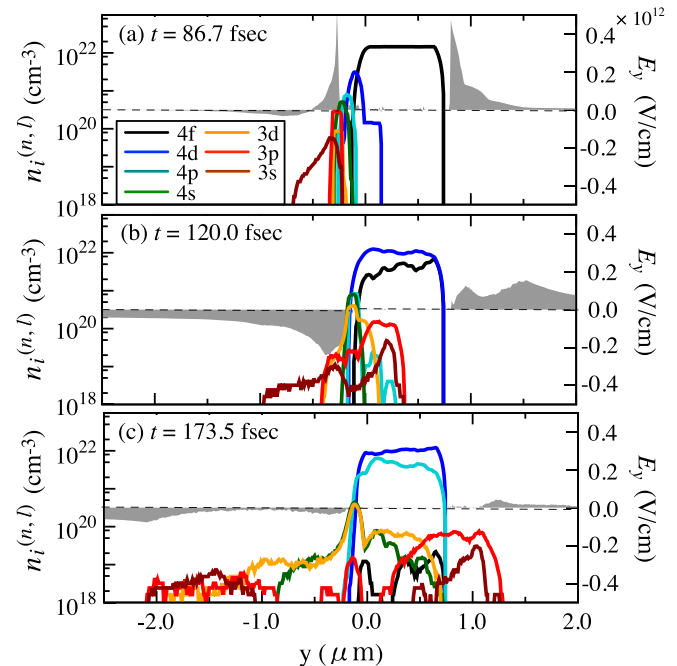

FIG. 5. Spatial ion distributions of (i) + (ii) + (iii) for each ion state (n, l) on a logarithmic scale and the electric field for laser propagation direction E_y represented by gray shading on a linear scale.

surface. Then, the laser ponderomotive force pushes the electrons into the inside of the film and excites the electrostatic field E_y as balancing to that. Although the charge-to-mass ratio of $q = 69$ (3s) is the highest value in this case, the peak amplitude of E_y is located around the distribution of 3p and preferentially accelerates the ions with 3p to the inside. When the ponderomotive force starts to decrease after the laser peak amplitude, the direction of E_y changes to $-y$ as a result of losing the force balance, as indicated in Fig. 5(b). Therefore, the accelerated ions are separated and propagate to the inside as an ion bunch with multiple charge states of $q = 32$ (4d)-69 (3s). When the ions reach the rear surface, only the front part of the ions with 3p and 3s is re-accelerated and co-propagates with the sheath field, as seen in Fig. 5(c).

Figure 6 represents the ion energy distribution for each n, l at 240 fs when the acceleration saturates. It is noted that the energy distribution is observed in the spatial region of $y > 0$ to evaluate the ion acceleration in the $+y$ direction. The ion distribution is clearly separated to the low-energy part of the bulk ions ($E_i \leq 2.0 \times 10^{-3}$ Mev/u) and the high-energy part of the accelerated ions ($E_i \geq 1.0 \times 10^{-2}$ Mev/u). In the high-energy part, the charged ions from $q = 32$ (4d) to $q = 69$ (3s) overlap in the region of $10^{-2} \leq E_i \leq 10^0$ MeV/u. The ion energy of $q = 67$ (3p) reaches the maximum value (i.e., 10.2 MeV/u), which is slightly larger than that of $q = 69$ (3s).

B. TNSA with the ionization process

Figure 7 illustrates the spatial ion density $n_i^{(n,l)}$ of (iv) and the longitudinal electric field E_y on a logarithmic scale. When the laser amplitude reaches the peak value, the electrostatic sheath field also reaches the maximum amplitude (i.e., $E_y = 0.5$ TV/cm) at the rear surface of the film. The sheath field ionizes the ions to $q = 67$ (3p) and accelerates them to the vacuum area. The location of the peak sheath amplitude co-propagates with the accelerated ion front so that the specific ions with $q = 67$ (3p) continue to be accelerated as long as E_y becomes negligibly small. Ions with lower charge states are also ionized behind the ion front. However, the lower charge distributions remain behind the sheath field with the propagation of the ion front. The
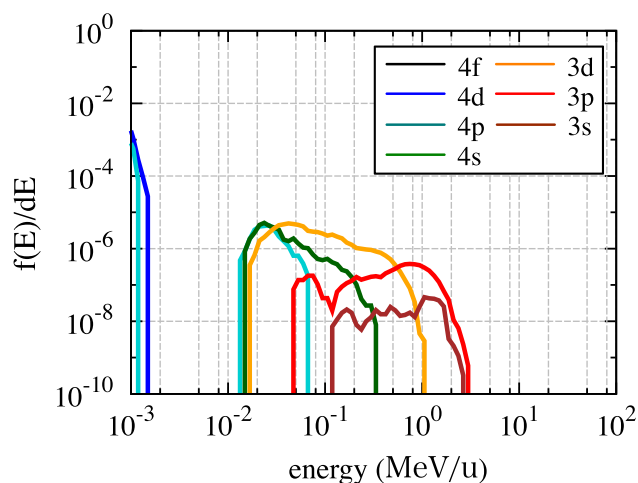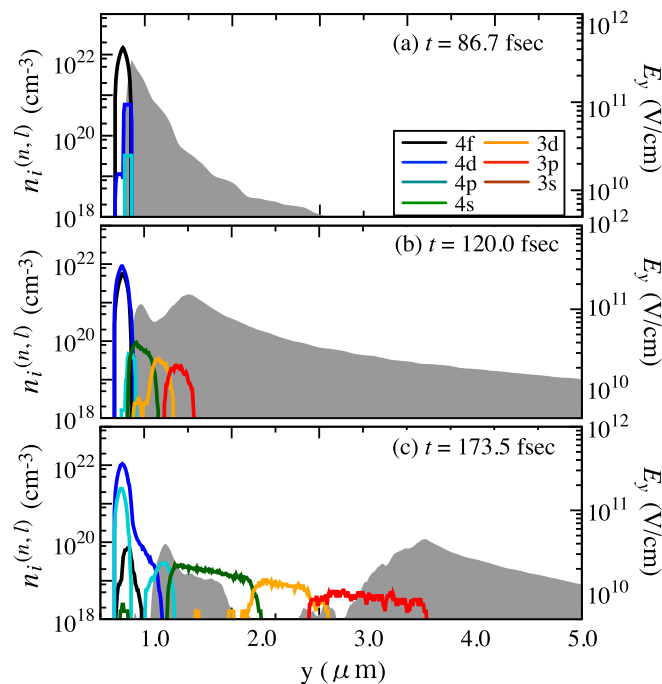
FIG. 7. Spatial ion distributions of (iv) for each ion state (n, l) and longitudinal electric field E_y on a logarithmic scale.

acceleration time of these ions becomes shorter than that of the ion front. On the other hand, the small electric field E_y, which is excited by bulk electrons at a cold temperature (i.e., $T_e \simeq$ keV), remains near the rear surface of the film. The field continues to accelerate the ion, keeping the charge states in $n = 4$. When the ions accelerating from the front surface pass through the rear, the sheath field begins to propagate with them. Thus, the ions behind the expanded front are also re-accelerated along with the ballistic ion propagation of RPA.

Figure 8 represents the ion energy distribution for each state (n, l) of (iv) on a logarithmic scale. The charge distributions of the accelerated ions are separately distributed within the range of
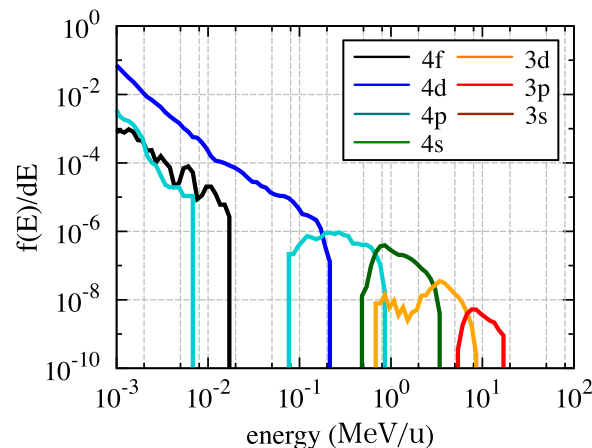
FIG. 6. Ion energy distribution of (i) + (ii) + (iii) for each ion state (n, l) at 240 fs.

FIG. 8. Ion energy distribution of (iv) for each ion state (n, l) at 240 fs.

$0.1 - 10\,\text{Mev/u}$. In this distribution, the energy of the highest charge state of (iv) [i.e., $q = 67$ (3p)] reaches $22.2\,\text{Mev/u}$, which is approximately two times higher than that from the front side (i). The distribution of $q = 55$ (3d)-62 (3p) is in the range of $1 - 10\,\text{Mev/u}$, which is considerably smaller than that of $q = 67$ (3p) even without the dependence of the charge-to-mass ratio.

IV. DEPENDENCE OF LASER INTENSITY FOR EACH IONIZATION AND ACCELERATION

For different laser intensities, the maximum ion energy from the rear surface $\epsilon_{i,\text{rear}}$ in TNSA is also larger than that from the front surface $\epsilon_{i,\text{front}}$ in hole-boring RPA. Figure 9 represents the maximum ion energies, $\epsilon_{i,\text{front}}$ and $\epsilon_{i,\text{rear}}$, for the representative laser intensities, respectively, where the highest charge state in each case is represented in each plot. Here, theoretical models proposed by Passoni *et al.*[26] and Sentoku *et al.*[28] are compared to the simulation results by assuming the highest charge state simulated in each mechanism. The ion acceleration from the front surface takes place after the laser field ionizes the ions to the highest charge state, as discussed in Sec. III. Thus, even if the constant charge state is substituted according to the scaling law, it reveals a similar dependence of the simulation results. However, the ion energy in the simulation results is slightly larger than the predicted energy due to re-acceleration coupled with the electric sheath field near the rear surface. Furthermore, a multiply charged ion from the rear surface is accelerated to a higher energy than that from the front surface in each case. From these simulation results, the energy scaling of the maximum ion energy $\epsilon_{i,\text{rear}}$ is estimated as $I^{0.533}$, which exceeds the scaling of $\epsilon_{i,\text{front}}$ (i.e., $I^{0.473}$). For this acceleration, the simulation result decreases to $60 - 80\%$ of the theoretical scaling. This is because the charge states near the rear surface are lower than the highest value until the sheath field with the peak amplitude ionizes them.

V. EFFECT OF THE CONTAMINATION LAYER FOR ACCELERATED AU ENERGY

A contamination layer of water vapor (H_2O) is expected to be attached to the film surface, and proton acceleration is caused by

this layer. On the front surface of the film, the contamination is peeled to the outside region by the direct laser interaction so that it is negligible for RPA. However, the energy of the sheath field generated on the rear surface is wasted in accelerating the contamination [i.e., proton (p) and oxygen (O)], and the acceleration energy of the Au ion decreases. In this case, the proton has the highest charge-to-mass ratio $(Z/M)_\text{p}$ even in the fully ionized state of the other ions [i.e., $(Z/M)_\text{p} \simeq 2.0(Z/M)_\text{O} \simeq 2.5(Z/M)_\text{Au}$]. The contaminated atoms also tend to be fully ionized compared with the Au atom, which has higher ionization potentials. Thus, both the field ionization degree and the acceleration energy of Au decrease through the energy transfer to p and O, which are readily accelerated from the rear surface by the sheath field. Figure 10 illustrates the ion energy distribution of Au from the front surface $\text{Au}_{(\text{rear})}$ and rear surface $\text{Au}_{(\text{rear})}$, as well as the distributions of p and O, which are initially located in front of the rear surface with a thickness of $10.0\,\text{nm}$ (a) and $20.0\,\text{nm}$ (b). In case (a), the proton energy reaches $31.0\,\text{MeV/u}$, which is the highest value in all ions. Most of the protons are also accelerated to over $20.0\,\text{MeV/u}$ and continue propagating in front of the ion distribution including O and Au. On the other hand, the ion energy of O is less than that of p due to the difference of the above-mentioned charge-to-mass ratio and reaches $22.8\,\text{MeV/u}$ with a fully ionized state. The maximum energy of $\text{Au}_{(\text{rear})}$ decreases to $5.6\,\text{MeV/u}$, which corresponds to approximately $1/4$ of that in the case of the pure gold film. Furthermore, the highest
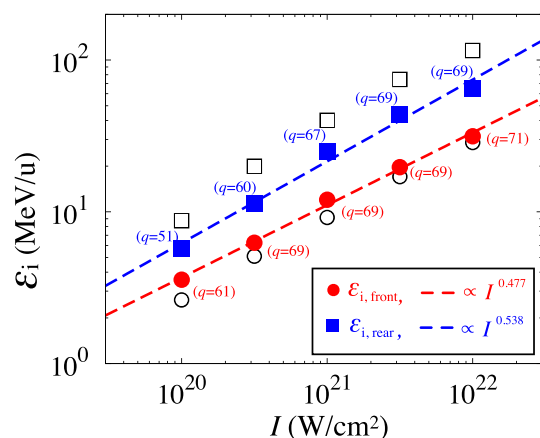

FIG. 9. Dependence of the maximum ion energies of TNSA (solid square) and hole-boring RPA (solid circle) on the laser intensity. The theoretical models proposed by Passoni *et al.* and Sentoku *et al.* are represented by empty squares and empty circles, respectively.
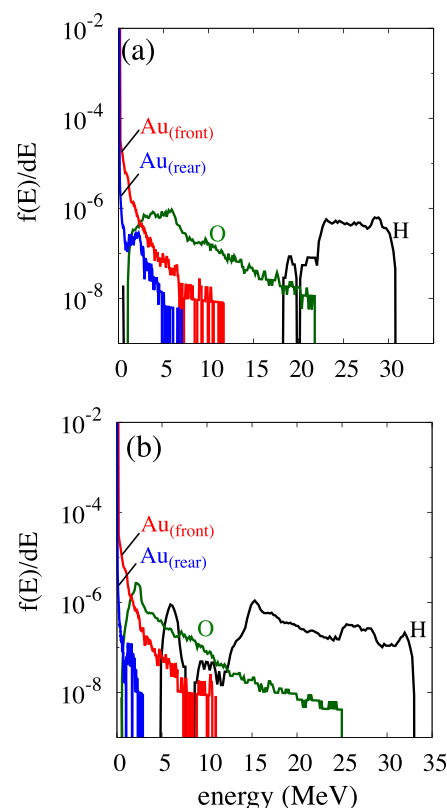

FIG. 10. Ion energy distribution of Au from the front surface $\text{Au}_{(\text{front})}$ and rear surface $\text{Au}_{(\text{rear})}$ and the distributions of p and O, which are initially located on the rear surface with a thickness of (a) $10.0\,\text{nm}$ and (b) $20.0\,\text{nm}$.

charge state of Au$_{(rear)}$ also decreases to $q = 58$ (3d) from $q = 67$ (3p) due to the Debye screening of the electric sheath field behind the contamination layer. The maximum energy from the front surface Au$_{(front)}$ is 10.6 MeV/u, which is the same as the energy without contamination. In Fig. 10(b), Au$_{(rear)}$ decreases to half the value of that in case (a) (i.e., 2.7 MeV/u). The maximum charge state corresponding to that decreases to $q = 51$ (4s). Even if the contamination thickness becomes larger than 20.0 nm, the energy distribution of Au$_{(front)}$ is the same as seen in Fig. 10(b). Therefore, both the ionization level and ion energy from the rear surface become less than those from the front surface.

VI. SCALING MODEL OF ION ENERGY WITH EACH CHARGE STATE IN TNSA

While the ion front with a high charge state is accelerated to the maximum energy in TNSA, the ions with a lower charge state are also accelerated. To describe the maximum ion energy for each charge state, we consider simplified scaling based on the electric field based on the tunnel ionization formula

$$E_q = \frac{U_q^2}{4qe^3},$$ (3)

where U_q is the ionization energy of charge state q and e is the electron elementary charge. The ionization model is also illustrated in Fig. 1 as the relationship between laser intensity and ionization potential for charge state q. This formula also represents the upper limit of the accelerating electric field for an ion with q (i.e., $E_{\lim,q} < E_{q+1}$). Around the rear surface, the charge state inside the film is determined following the Debye screening of the sheath field (i.e., $E_y(y) = E_p e^{-(l_s-y)/\lambda_D}$), as illustrated in Fig. 11. Here, l_s corresponds to the film thickness, E_p is the peak amplitude of the sheath field on the rear surface, and λ_D [$= \sqrt{T_e/(e^2 n_e)}$] is the Debye length inside the film. The number of ions ionized by the field ionization is small compared with that ionized by the impact ionization. Therefore, the Debye length around the rear surface λ_D is approximated to a constant value based on the average electron temperature and average charge density. In this field profile, the ion velocity $v_q(t)$ is calculated from the equation of motion described by

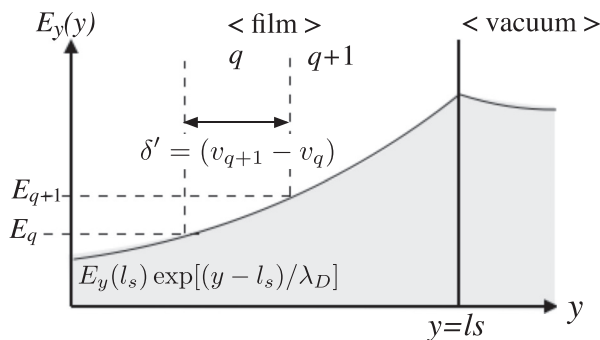$$v_q(t) = \frac{qe}{M_i} \int_0^{\tau_q} dt E_y(y),$$ (4)

FIG. 11. Schematic representation of Debye screening of the sheath field and charge distributions around the rear surface of the film.

where M_i is the ion mass and τ_q is the acceleration time. For the ion peak energy with q, the ions locate closely behind the $q + 1$ region at initial and receive the electric field with almost E_{q+1}. The ions are emitted co-propagating with the sheath field from the order of the high charge state. Therefore, the accelerating electric field for q is written by $E_y(t) = E_{q+1} e^{(-(v_{q+1}-v_q)t/\lambda_d)}$. Here, we assume that the ions with q are accelerated until the relative distance reaches the Debye length, i.e.,

$$(v_{q+1}(t) - v_q(t))\tau_q = \lambda_D.$$ (5)

The spatial location of q is close to that of $q + 1$ so that the electric field for q and $q + 1$ is assumed to be the same value. Thus, the acceleration length for the maximum ion energy of q is approximated from Eqs. (2) and (3) as follows:

$$v_q(t)\tau_q = \frac{v_q(t)}{v_{q+1}(t) - v_q(t)}\lambda_D \simeq q\lambda_D.$$ (6)

Here, the acceleration time is significantly shorter than the time at which the electric field amplitude weakens with ion expansion. For maximum ion energy, the ion with q is located at the interface between the distributions of q and $q + 1$. Thus, the electric field is approximated as a constant value based on E_{q+1} during the acceleration time τ_q, i.e., $E_{q,\max} = E_{q+1}/2$. Then, the maximum ion energy of q is given by

$$\epsilon_{i,\max}^q = \frac{q}{M_i} \int_0^{v_q\tau_q} dy E_y(y) \simeq \frac{1}{2} q^2 \lambda_D E_{q+1}.$$ (7)

It is rewritten for the ionization energy using Eq. (1),

$$\epsilon_{i,\max}^q = \frac{1}{2} \frac{q}{4e^3} \lambda_D U_{q+1}.$$ (8)

This reveals the maximum ion energy for each charge state in that the field ionization is dominant.

Figure 12 presents the simulation results of the maximum ion energies at laser intensities of $I = 10^{20}, 10^{21},$ and 10^{22} W/cm^2 and the scaling formula (6). Here, the charge dependence of the ion energy is compared in the cases without a contamination layer (a) and with 10 nm thickness (b). Debye lengths for $I = 10^{20}, 10^{21},$ and 10^{22} W/cm^2 are 26.1 nm, 26.8 nm, and 25.2 nm, which are calculated from the simulation results of the average temperature and average electron density, respectively. Here, λ_D is approximated to 26.0 nm for the modeling. In case (a), the ions on the expanded front are predominately accelerated to higher energy above the scaling formula (6). This is because the front with the sheath field continues to be accelerated beyond the acceleration length assumed in Eq. (3). Behind the ion front, ions with a lower charge state are also accelerated according to the upper limit of each ionization potential as the relation (6). Even for different laser intensities, the maximum ion energy for the lower charge state is explained by this formula, as illustrated in Fig. 12(a). In case (b), this scaling explains the charge dependence of the maximum ion energy, including the maximum ion energy, as illustrated in Fig. 12(b). The protons and oxygen ions are accelerated ahead of the Au ions by the initial locations in front of the Au film and the higher charge to mass ratio than that of Au. Then, the front of the sheath field co-propagates with the proton expansion so that the acceleration length described by Eq. (3) is
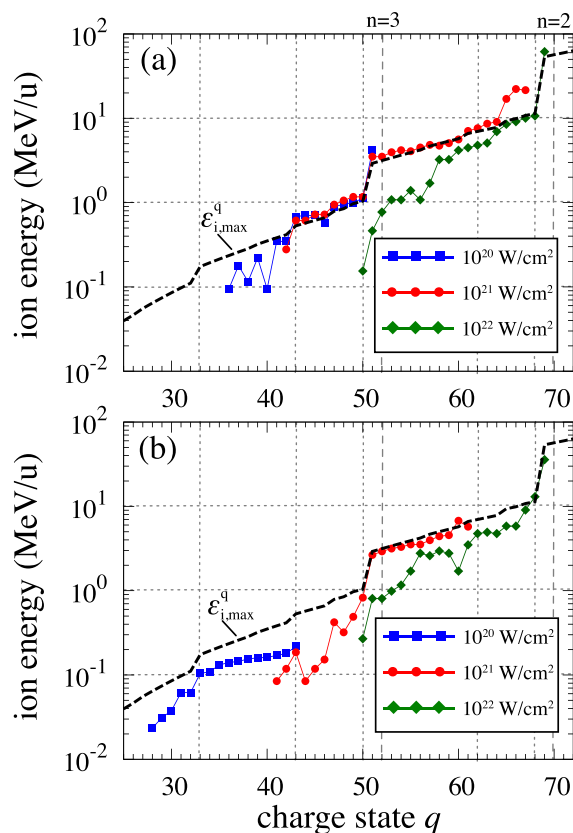
FIG. 12. Maximum ion energies for each charge state at laser intensities of $I = 10^{20}$, 10^{21}, and 10^{22} W/cm² and the scaling formula (6). The charge dependence of the ion energy is compared in case (a) without contamination and (b) with a 10 nm contamination thickness.

applicable to the highest energy of the accelerated Au ions. However, for a laser intensity of $I = 10^{20}$ W/cm², the ion energy becomes less than the scaling (6). This is because that the field amplitude accelerating the ions is smaller than the amplitude predicted by the field ionization, and the ionization type changes the electron impact.

For a lower-Z atom, when the ions are ionized to a fully ionized state, the ion energy becomes higher than the energy expected by this scaling. For a lower laser intensity and a longer pulse duration, the ions remain on the film surface in a longer time, and the collision can address the ionization to the higher charge state of the accelerated ion. The applicable range of the charge state in this modeling is expected to decrease in order from the lower charge state, which is ionized by the collision. Therefore, this scaling model is limited in the following conditions: (1) the accelerated ions are not a fully ionized state, (2) the outer charge state of the accelerated ion is ionized by the field process, and (3) the ion acceleration time corresponding to the laser pulse duration is short enough to assume that the Debye length around the rear surface is constant before the collisional ionization takes place.

VII. COLLISIONAL EFFECT AND THREE-BODY RECOMBINATION

To investigate the collisional effect for ion acceleration, we compare the spatial distributions of the ions ionized by the field and the

electron impact. These ion distributions, which are categorized by each ionization component for the outer charge states of the ions, and the average ion energy $\langle E_i(y) \rangle$ are shown in Fig. 13. The time of these results is chosen to be $t = 500$ fs when the ion acceleration and ionization process mostly saturate in the cases of both $I_l = 1.0 \times 10^{20}$ W/cm² (a) and $I_l = 1.0 \times 10^{21}$ W/cm² (b). It is noted that each component is unrelated to the previous ionization process of each ion. In case (a), the ions ionized by the electron impact are distributed in the range of $y = 0.0\ \mu m - 2.0\ \mu m$, which is behind that ionized by the field. The average ion energy of the electron impact component reaches only $\langle E_i \rangle \simeq 5.8 \times 10^{-2}$ MeV/u, while the maximum ion energy reaches $\langle E_i \rangle \simeq 4.0$ MeV/u. In case (b), the region of the electron impact component extends to $y = 3.5\ \mu m$, and the average energy increases to $\langle E_i \rangle \simeq 7.2 \times 10^{-1}$ MeV/u. In both (a) and (b), these energies are approximately two orders of magnitude smaller than the maximum ion energy. In the time scale in which the ions hardly expand from the rear surface, the electric sheath field E_y ionizes the higher charge state before electron impact ionization occurs. When the electron impact ionizes to a higher charge state, which is estimated to be approximately $(n_e v_e \sigma_{im,(n=3)})^{-1} \simeq 800$ fs, the accelerated ions are already expanded to the vacuum region at such irradiated laser intensities.

At the later time, the three-body recombination process proceeds in a high-density plasma composed of heavy atoms. For estimating this effect for ion acceleration, the ratio between the three-body recombination and electron impact ionization is evaluated by the Saha–Boltzmann equation[38] as follows:

$$\frac{\sigma_R}{\sigma_I} = n_e \frac{g_q}{g_{q+1}} \frac{h^3}{(2\pi m_e T_e)^{3/2}} \exp\left[\frac{U_q}{T_e}\right], \qquad (9)$$
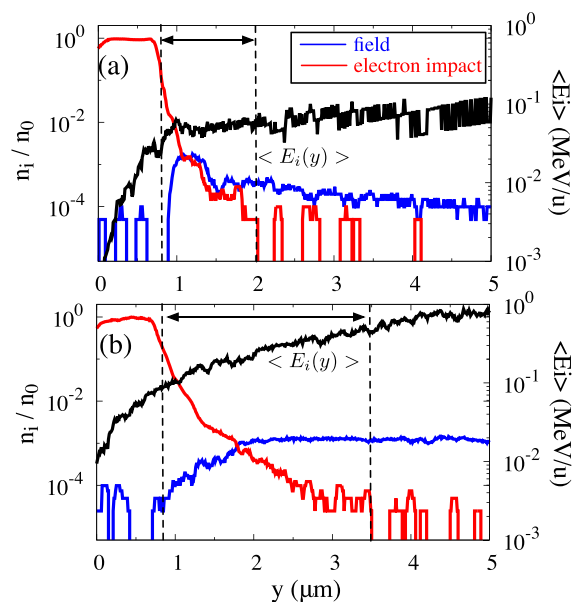

FIG. 13. Spatial distributions of the ion density ionized by the field (blue line) and electron impact (red line) and the average ion energy (black line) in the case of (a) $I_l = 1.0 \times 10^{20}$ W/cm² and (b) $I_l = 1.0 \times 10^{21}$ W/cm².
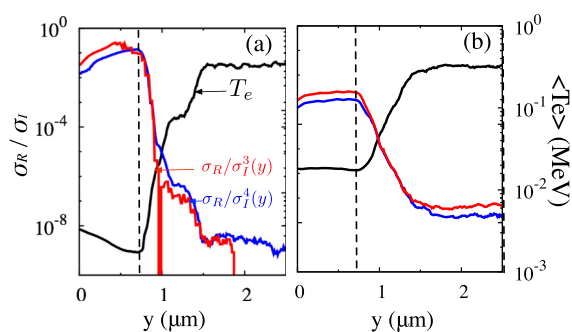
FIG. 14. Spatial distributions of $\sigma_R/\sigma_I^n(y)$ averaged for every quantum number as a red line ($n=3$) and a blue line ($n=4$) and the average electron temperature $T_e(y)$ as a black line around the rear surface in each case of (a) $I = 1.0 \times 10^{20}$ W/cm^2 and (b) $I = 1.0 \times 10^{21}$ W/cm^2.

where σ_R and σ_I are the three-body recombination rate and ionization rate for charge state q, respectively, h is Planck's constant, and g_q is the statistical weight, which corresponds to degeneracy for the state q. Here, the post-process estimation is calculated from the simulation results of the electron density and electron temperature in the moving frame of the average ion velocity for each spatial mesh. Figure 14 shows the spatial distributions of the average ratio of each quantum number as $\sigma_R/\sigma_I^n(y)$ and the electron temperature $T_e(y)$ at $t = 500$ fs in the case of $I_l = 1.0 \times 10^{20}$ W/cm^2 (a) and $I_l = 1.0 \times 10^{21}$ W/cm^2 (b). At this time, all ions are already ionized more than $n=4$ in both cases; thus, this estimation is only applied for $n=3$ and $n=4$. In case (a), the average electron temperature is approximately $T_e = 4.0$ keV, and the recombinations of both quantum numbers affect only $\sigma_R/\sigma_I^{n=3,4}(y) \simeq 0.1$, even in the film region ($0\,\mu m \leq y < 0.8\,\mu m$). The ratios drastically decrease with ion expansion to $\sigma_R/\sigma_I^{n=3,4} \simeq 10^{-9}$ ($0.8\,\mu m \leq y$).

In case (b), the average electron temperature in the film region increases to $\langle T_e \rangle = 30.0$ keV. Thus, both ratios of $n=3$ and 4 decrease to $\sigma_R/\sigma_I^{n=3,4} \simeq 4.0 \times 10^{-3}$, which indicates that electron impact ionization becomes dominant by increasing the irradiated laser intensity. In the outside region ($y \geq 0.8\,\mu m$), the average electron temperature exponentially increases to $T_e = 400.0$ keV, which is nearly identical to that in case (a). The ratios of both are only $\sigma_R/\sigma_I^{n=3,4} \simeq 10^{-8}$. Considering that each ion ionized by the electron impact propagates to $y = 2.0\,\mu m$ and $y = 3.5\,\mu m$, as illustrated in Fig. 13, the recombination effect is sufficiently small to be negligible for the accelerated mechanism.

VIII. CONCLUSION

In this paper, we investigate the ionization process and acceleration mechanism of Au ions from a substrate film interacting with relativistic high intensity ($I = 10^{20} - 10^{22}$ W/cm^2) and a short-pulse ($\tau_l = 40$ fs) laser by using particle-in-cell simulations, which include field ionization and electron impact ionization. In these cases, RPA and TNSA are dominant in emitting highly charged Au ions ($q > 50$) with high energy ($\simeq 10$MeV/u) from the front and rear surfaces of the film, respectively. The electrostatic field excited in each mechanism ionizes the atoms to a high charge state through field ionization dynamics and accelerates these ions to the rear side vacuum area. The

accelerated ion energies are characterized by the charge-to-mass ratio and spatial distributions of the multiple charge states corresponding to the electric field profile. These properties are discussed in Sec. III and summarized as follows.

In RPA, for a laser intensity of $I = 10^{21}$ W/cm^2, the laser field directly ionizes the atoms to a charge state $q = 69$ (3s). Then, the electrostatic field balancing the laser ponderomotive force accelerates the charged ions to the inside of the film. These ions ballistically propagate, keeping their charge state to the rear surface. Then, ions bunching from $q = 32$ (4d) to $q = 69$ (3s) are emitted with an energy range of 0.01 MeV/u–5.0 MeV/u. The front of the ion bunch is re-accelerated by the sheath field on the rear surface, and the maximum ion energy reaches 10.8 MeV/u.

In TNSA, for a laser intensity of $I = 10^{21}$ W/cm^2, the sheath field excited on the rear surface of the film ionizes the atoms to $q = 67$ (3p). Then, the field accelerates them to 22.2 MeV/u. The maximum ion energy of $q = 67$ (3p) is much larger than that of the lower charge state, even without the dependence of the charge-to-mass ratio. This is because the peak amplitude of the sheath field co-propagates with the front of the accelerated ion distribution with $q = 67$ (3p).

From the dependence of the maximum ion energy on the irradiated laser intensity, it is determined that the energy scaling of TNSA (i.e., $I^{0.533}$) is larger than that of hole-boring RPA (i.e., $I^{0.473}$) only in the case of the pure gold film. However, the energy distribution is found to be influenced by the existence of contamination, such as water vapor (H$_2$O). In this case, the attachment of a layer with the thickness over 10 nm at the rear surface suppresses the acceleration of the Au ions and reverses the relation of the ion energies from both surfaces since the sheath field readily accelerates the protons and oxygen, as discussed in Sec. V.

For TNSA, we successfully derive the theoretical scaling of the maximum ion energy for each charge state, as discussed in Sec. VI. It is based on the electric field of the classical tunnel ionization formula as the upper limit of the field accelerating the ions. In addition, it correctly describes the simulation results of the maximum ion energies in the range in which the field ionization dominantly takes place.

For the laser intensities of $I = 10^{20} - 10^{22}$ W/cm^2, it is found that the accelerated ions are mainly ionized by field ionization, while electron impact ionization takes place only in the film region. Thus, the collisional and recombination processes are negligible for the accelerated high-energy ions in the present case, as discussed in Sec. VII. However, at a lower laser intensity such as $I < 10^{19}$ W/cm^2 and longer pulse duration, the electron impact ionizes atoms to high-charge states, as well as those of the field ionization. With such a collision, the energy loss due to the bremsstrahlung emission is not negligible to evaluate the resultant ionization and the ion acceleration. In addition to these collisional effects, at a higher energy laser field, the shock wave acceleration is expected to contribute both the ionization and the ion acceleration. It is interesting to study heavier ion acceleration with more complex atomic processes and acceleration mechanisms, and we plan to discuss these properties in a subsequent paper.

REFERENCES

[1] S. C. Wilks, A. B. Langdon, T. E. Cowan, M. Roth, M. Singh, S. Hatchett, M. H. Key, D. Pennington, A. MacKinnon, and R. A. Snavely, Phys. Plasmas **8**, 542–549 (2001).

[2] H. Schwoerer, S. Pfotenhauer, O. Jäckel, K.-U. Amthor, B. Liesfeld, W. Ziegler, R. Sauerbrey, K. W. D. Ledingham, and T. Esirkepov, Nature **439**, 445–448 (2006).

[3] M. Nishiuchi, A. Fukumi, H. Daido, Z. Li, A. Sagisaka, K. Ogura, S. Orimo, M. Kado, Y. Hayashi, M. Mori, S. Bulanov, T. Esirkepov, K. Nemoto, Y. Oishi, T. Nayuki, T. Fujii, A. Noda, Y. Iwashita, T. Shirai, and S. Nakamura, Phys. Lett. A **357**, 339–344 (2006).

[4] L. Robson, P. T. Simpson, R. J. Clarke, K. W. D. Ledingham, F. Lindau, O. Lundh, T. McCanny, P. Mora, D. Neely, C.-G. Wahlström, M. Zepf, and P. McKenna, Nat. Phys. **3**, 58–62 (2007).

[5] H. Daido, M. Nishiuchi, and A. S. Pirozhkov, Rep. Prog. Phys. **75**, 056401 (2012).

[6] S. V. Bulanov and V. S. Khoroshkov, Plasma Phys. Rep. **28**, 453–456 (2002).

[7] S. Fritzler, V. Malka, G. Grillon, J. P. Rousseau, F. Burgy, E. Lefebvre, E. D'Humières, P. McKenna, and K. W. D. Ledingham, Appl. Phys. Lett. **83**, 3039–3041 (2003).

[8] M. Roth, T. E. Cowan, M. H. Key, S. P. Hatchett, C. Brown, W. Fountain, J. Johnson, D. M. Pennington, R. A. Snavely, S. C. Wilks, K. Yasuike, H. Ruhl, F. Pegoraro, S. V. Bulanov, E. M. Campbell, M. D. Perry, and H. Powell, Phys. Rev. Lett. **86**, 436–439 (2001).

[9] M. T. S. Atzeni and J. Honrubia, Nucl. Fusion **42**, L1 (2002).

[10] E. L. Clark, K. Krushelnick, M. Zepf, F. N. Beg, M. Tatarakis, A. Machacek, M. I. K. Santala, I. Watts, P. A. Norreys, and A. E. Dangor, Phys. Rev. Lett. **85**, 1654–1657 (2000).

[11] M. Nishiuchi, H. Sakaki, S. Maeda, A. Sagisaka, A. S. Pirozhkov, T. Pikuz, A. Faenov, K. Ogura, M. Kanasaki, K. Matsukawa, T. Kusumoto, A. Tao, T. Fukami, T. Esirkepov, J. Koga, H. Kiriyama, H. Okada, T. Shimomura, M. Tanoue, Y. Nakai, Y. Fukuda, S. Sakai, J. Tamura, K. Nishio, H. Sako, M. Kando, T. Yamauchi, Y. Watanabe, S. V. Bulanov, and K. Kondo, Rev. Sci. Instrum. **85**, 02B904 (2014).

[12] M. Nishiuchi, H. Sakaki, T. Z. Esirkepov, K. Nishio, T. A. Pikuz, A. Y. Faenov, I. Y. Skobelev, R. Orlandi, H. Sako, A. S. Pirozhkov, K. Matsukawa, A. Sagisaka, K. Ogura, M. Kanasaki, H. Kiriyama, Y. Fukuda, H. Koura, M. Kando, T. Yamauchi, Y. Watanabe, S. V. Bulanov, K. Kondo, K. Imai, and S. Nagamiya, Phys. Plasmas **22**, 033107 (2015).

[13] W. Scheid, H. Müller, and W. Greiner, Phys. Rev. Lett. **32**, 741–745 (1974).

[14] K. W. D. Ledingham, J. Magill, P. McKenna, J. Yang, J. Galy, R. Schenkel, J. Rebizant, T. McCanny, S. Shimizu, L. Robson, R. P. Singhal, M. S. Wei, S. P. D. Mangles, P. Nilson, K. Krushelnick, R. J. Clarke, and P. A. Norreys, J. Phys. D: Appl. Phys. **36**, L79–L82 (2003).

[15] V. Malka, S. Fritzler, E. Lefebvre, M.-M. Aleonard, F. Burgy, J.-P. Chambaret, J.-F. Chemin, K. Krushelnick, G. Malka, S. P. D. Mangles, Z. Najmudin, M. Pittman, J.-P. Rousseau, J.-N. Scheurer, B. Walton, and A. E. Dangor, "Electron acceleration by a wake field forced by an intense ultrashort laser pulse," Science **298**, 1596–1600 (2002).

[16] F. Ewald, H. Schwoerer, S. Düsterer, R. Sauerbrey, J. Magill, J. Galy, R. Schenkel, S. Karsch, D. Habs, and K. Witte, "Application of relativistic laser plasmas for the study of nuclear reactions," Plasma Phys. Controlled Fusion **45**, A83–A91 (2003).

[17] K. Nemoto, A. Maksimchuk, S. Banerjee, K. Flippo, G. Mourou, D. Umstadter, and V. Y. Bychenkov, Appl. Phys. Lett. **78**, 595–597 (2001).

[18] K. W. D. Ledingham, P. McKenna, T. McCanny, S. Shimizu, J. M. Yang, L. Robson, J. Zweit, J. M. Gillies, J. Bailey, G. N. Chimon, R. J. Clarke, D. Neely, P. A. Norreys, J. L. Collier, R. P. Singhal, M. S. Wei, S. P. D. Mangles, P. Nilson, K. Krushelnick, and M. Zepf, J. Phys. D: Appl. Phys. **37**, 2341–2345 (2004).

[19] A. J. Mackinnon, Y. Sentoku, P. K. Patel, D. W. Price, S. Hatchett, M. H. Key, C. Andersen, R. Snavely, and R. R. Freeman, Phys. Rev. Lett. **88**, 215006 (2002).

[20] M. Kaluza, J. Schreiber, M. I. K. Santala, G. D. Tsakiris, K. Eidmann, J. Meyer-ter Vehn, and K. J. Witte, Phys. Rev. Lett. **93**, 045003 (2004).

[21] E. D'Humières, E. Lefebvre, L. Gremillet, and V. Malka, Phys. Plasmas **12**, 062704 (2005).

[22] L. O. Silva, M. Marti, J. R. Davies, R. A. Fonseca, C. Ren, F. S. Tsung, and W. B. Mori, "Proton shock acceleration in laser-plasma interactions," Phys. Rev. Lett. **92**, 015002 (2004).

[23] J. H. Bin, M. Yeung, Z. Gong, H. Y. Wang, C. Kreuzer, M. L. Zhou, M. J. V. Streeter, P. S. Foster, S. Cousens, B. Dromey, J. Meyer-ter Vehn, M. Zepf, and J. Schreiber, Phys. Rev. Lett. **120**, 074801 (2018).

[24] P. Mora, Phys. Rev. Lett. **90**, 185002 (2003).

[25] P. Mora, Phys. Rev. E **72**, 056401 (2005).

[26] M. Passoni, V. T. Tikhonchuk, M. Lontano, and V. Y. Bychenkov, Phys. Rev. E **69**, 026411 (2004).

[27] M. Passoni and M. Lontano, Phys. Rev. Lett. **101**, 115001 (2008).

[28] Y. Sentoku, T. E. Cowan, A. Kemp, and H. Ruhl, "High energy proton acceleration in interaction of short laser pulse with dense plasma target," Phys. Plasmas **10**, 2009–2015 (2003).

[29] A. Henig, S. Steinke, M. Schnürer, T. Sokollik, R. Hörlein, D. Kiefer, D. Jung, J. Schreiber, B. M. Hegelich, X. Q. Yan, J. Meyer-ter Vehn, T. Tajima, P. V. Nickles, W. Sandner, and D. Habs, Phys. Rev. Lett. **103**, 245003 (2009).

[30] T. Esirkepov, M. Borghesi, S. V. Bulanov, G. Mourou, and T. Tajima, Phys. Rev. Lett. **92**, 175003 (2004).

[31] D. Kawahito and Y. Kishimoto, Phys. Plasmas **24**, 103105 (2017).

[32] T. Auguste, P. Monot, L. A. Lompre, G. Mainfray, and C. Manus, J. Phys. B **25**, 4181–4194 (1992).

[33] V. K. M. V. Ammosov and N. B. Delone, Sov. Phys. JETP **64**, 6 (1986).

[34] Y.-K. Kim and M. E. Rudd, Phys. Rev. A **50**, 3954–3967 (1994).

[35] T. Takizuka and H. Abe, J. Comput. Phys. **25**, 205–219 (1977).

[36] Y. Sentoku and A. Kemp, J. Comput. Phys. **227**, 6846–6861 (2008).

[37] L. Spitzer and R. Härm, Phys. Rev. **89**, 977–981 (1953).

[38] M. N. Saha, Proc. R. Soc. London Ser. A **99**, 135–153 (1921).